Geotechnical Testing Journal, Vol. 28, No. 2
Paper ID GTJ12595
Available online at: www.astm.org

Jong-Sub Lee[1] *and J. Carlos Santamarina*[2]

P-Wave Reflection Imaging

ABSTRACT: The reflection of elastic waves from interfaces is a robust phenomenon extensively used by animals (bats and dolphins), nondestructive techniques, and medical diagnosis. This study addresses the design and implementation of P-wave reflection imaging to evaluate the internal variability in small-scale submerged, soil models. The performance of this technology depends on fundamental aspects of P-wave propagation in soils, the selection of optimal P-wave transducers, and the development of an adequate test methodology. Design issues include transducer directivity, noise, axial resolution, near field effects, and proper thickness of the coupling water layer. The operating frequency is determined by transducer selection and affects the axial and lateral resolution, skin depth, near field, and divergence; high damping transducers permit higher axial resolution. In addition, data gathering must take into consideration temporal and spatial aliasing. Results show that P-wave reflection is a valuable tool to detect subsurface anomalies and layers, to assess phenomena such as slurry sedimentation, and to monitor the evolution of subsurface structures such as soil layers during liquefaction. Gradual changes in impedance, such as in slurry sedimentation, may prevent reflections.

KEYWORDS: directivity, liquefaction, near field, nondestructive testing, spatial resolution, sedimentation, subsurface monitoring, ultrasound transducer, variability

Introduction

P-wave reflection imaging has been extensively used in nondestructive testing (such as metal flaw detection, Mclntire 1991), underwater navigation, marine seismic (Waters 1992; Sheriff and Geldard 1995), and medical diagnosis (Gomm and Mauseth 1999). The technique is based on received time series that result from multiple reflections at interfaces and other internal heterogeneities.

P-wave reflection images can be effective to study geo-processes and systems such as scouring, hydraulic fill and land reclamation, and forensic analysis of marine structures. Both field-scale and model-scale implementations are possible. The difference between model and field scale applications is frequency. Medical applications operate at frequencies higher than 4 MHz (up to 15 MHz), and the maximum imaging depth is a few centimeters. On the other hand, relatively low frequencies are used for marine seismics (< 100 Hz) to attain higher exploration depth. While physical concepts are scalable, i.e., governing dimensional ratios apply at all scales, the nature of material-wave interaction may change with frequency (e.g., Biot relaxation—Biot 1956).

The goal of this study is to develop a high resolution P-wave imaging system to assess internal variability in submerged small-scale soil models. This paper includes a review of P-wave propagation, the selection of optimal P-wave transducers, the development of an adequate data gathering methodology, and a unique series of tests conducted to explore the potential of this tool.

P-Waves in Soils

P-wave velocity (Table 1), skin depth, and reflection at interfaces depend on soil parameters (for a detailed review, see Santamarina et al. 2001). The velocity of the longitudinal P-wave V_p in an infinite continuum is

$$V_P = \sqrt{\frac{M}{\rho}} = \sqrt{\frac{B + \frac{4}{3}G}{\rho}} \tag{1}$$

where M, B, and G are the constraint, bulk, and shear moduli, and ρ is the mass density. The shear modulus of the saturated soil is not affected by the presence of the fluids, i.e., $G_{soil} = G_{sk}$. On the other hand, the bulk modulus of the saturated soil B_{soil} combines the bulk modulus of the skeleton B_{sk}, the water B_w, and the mineral that makes the grains B_g,

$$B_{soil} = B_{sk} + \frac{1}{\frac{1}{B_w} + \frac{1-n}{B_g}} \tag{2}$$

where n is the soil porosity. Likewise, the mass density of the saturated soil ρ_{soil} depends on the mass density of the mineral ρ_g and the water ρ_w,

$$\rho_{soil} = (1-n)\rho_g + n\rho_w \tag{3}$$

Therefore, the P-wave velocity in the soil-water mixture is

$$V_{P\text{-}soil} = \sqrt{\frac{\left(B_{sk} + \frac{4}{3}G_{sk}\right) + \left(\frac{n}{B_w} + \frac{1-n}{B_g}\right)^{-1}}{(1-n)\rho_g + n\rho_w}} \tag{4}$$

Equation 4 is the Biot-Gassmann low frequency asymptotic solution.

P-wave impedance is defined as $z = \rho V$. Impedance mismatch determines the amplitude of reflections at interfaces. The variation in soil P-wave velocity and impedance are plotted versus porosity in Fig. 1. While the P-wave velocity initially decreases as porosity decreases from $n = 1.0$, the impedance remains always above 1.0. This observation is important to the application of P-wave imaging in high porosity clayey sediments.

Received February 25, 2004; accepted for publication July 22, 2004; published March 2005.

[1] Postdoctoral Fellow, Civil and Environmental Engineering, Georgia Institute of Technology, Atlanta, GA 30332.

[2] Professor, Civil and Environmental Engineering, Georgia Institute of Technology, Atlanta, GA 30332.

TABLE 1—*Nominal P-wave velocity, density, and impedance.*

	P-wave Velocity V_P [m/s]	Density ρ [kg/m^3]	Impedance $= \rho V_P$ [kg/m^{2}s] 10^6
Air (20°C, 1 atm)	343	1.204	0.0004
Deionized water	1480	998	1.5
Seawater	1531	1025	1.6
Sand (dry)*	150	1700	0.26
Clay (saturated)*	1500	1200	1.8
Ice	3500	917	3.2
Wood	4100	800	3.3
Plexiglass	2700	1200	3.2
Piezoceramic (PZT)	4000	7500	30
Aluminum	6400	2700	17.3
Lead	1900	11400	22
Copper	5000	8930	45
Steel	5900	7900	47
Nickel	5500	8850	49

Note: * Wave velocity and density of soils corresponds to ~100 kPa confinement.

Sources: Carmichael (1982, 1989); Guéguen and Palciauskas (1994); Santamarina et al. (2001); Weast (1988); Zagzebski (1986).

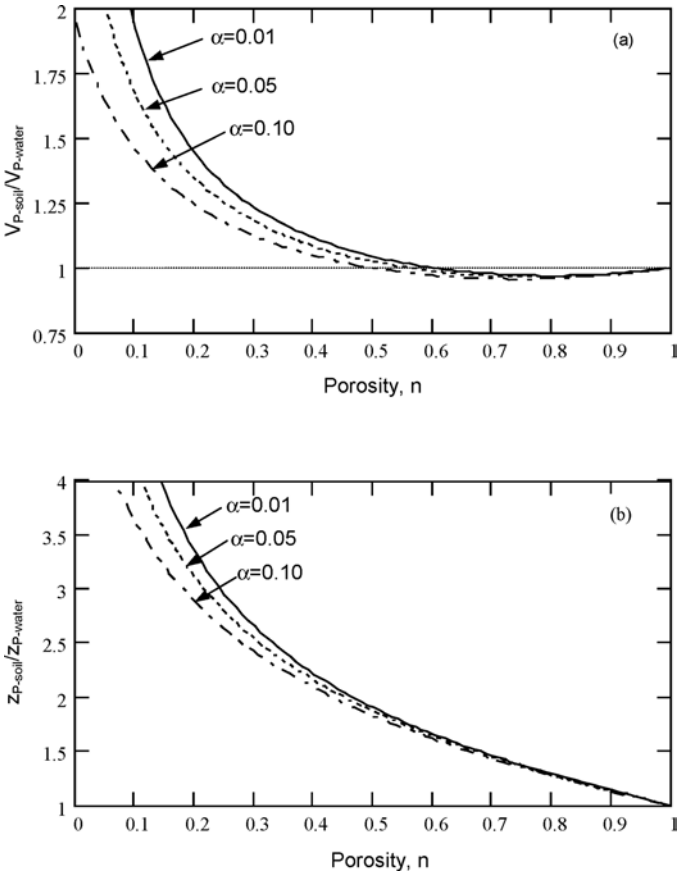

FIG. 1—*Normalized P-wave velocity (a) and impedance (b) versus porosity. The parameter* $\alpha = B_w/B_g$*, where* B_w *and* B_g *are the bulk modulus of the water and the mineral that makes the grains.*

Reflection and Transmission

When a plane wave impinges normal to an interface between Medium 1 with Impedance z_1 and Medium 2 with Impedance z_2, the reflection R and transmission coefficients $T = 1 + R$ for the pressure amplitude are (Wells 1979; Zagzebski 1996),

$$R = \frac{z_2 - z_1}{z_2 + z_1} \tag{5}$$

$$T = \frac{2z_2}{z_2 + z_1} \tag{6}$$

While normal incidence produces reflected and transmitted waves, the oblique incidence adds mode conversion, whereby reflected and transmitted waves of different propagation mode are generated (see Aki and Richards 1980 for a detailed analysis).

Resolution and Skin Depth

The wavelength λdepends on the propagation velocity V and the frequency f, i.e., $\lambda = V/f$. The size of the anomaly that can be resolved is of the same order of magnitude as the wavelength or larger. Therefore, higher resolution may be attained with higher frequency. Two types of resolution can be distinguished in P-wave reflection imaging:

- Axial resolution is the capability of detecting the spacing of anomalies in the radiation direction. High frequency and short duration are required to attain high axial resolution.
- Lateral resolution is the capability of distinguishing anomalies in the transverse direction (Zagzebski 1986). Therefore, lateral resolution is not only dependent on the signal frequency but also transducer size and directivity. Details are discussed in the near field and directivity sections.

The ability to detect an anomaly at a given depth, or sensitivity, depends on the amplitude of the reflected signal. Attenuation (α) reduces the signal amplitude as it propagates. The amplitude of a plane wave decreases in $1/e$ in a distance S_d

$$S_d = \frac{1}{\alpha} = \frac{V}{2\pi \cdot D \cdot f} \tag{7}$$

where S_d is known as the skin depth and D is the damping ratio. While resolution increases with increasing frequency, the skin depth decreases.

Ultrasonic Transducers: Selection and Characterization

The selection of the transducer is conditioned by the desired operating frequency, and plays a crucial role for attaining adequate P-wave reflection images. Other important transducer and installation characteristics include near field, directivity, axial resolution, shielding, and thickness of the coupling layer. These characteristics are evaluated next.

Structure of a P-wave Transducer—Ringing

The typical structure of an ultrasonic transducer is schematically shown in Fig. 2*a*. The transducer is composed of a piezoelectric element, a backing block, a matching layer, and an insulating casing. Selection guidelines follow.

Piezoelectric Material—The piezoelectric element converts electric energy into mechanical vibration and vice versa. An electric impulse makes the piezoelectric material ring at the resonant frequency, which is inversely proportional to the thickness of the piezoelectric material (thickness is ~λ/2 depending on boundary

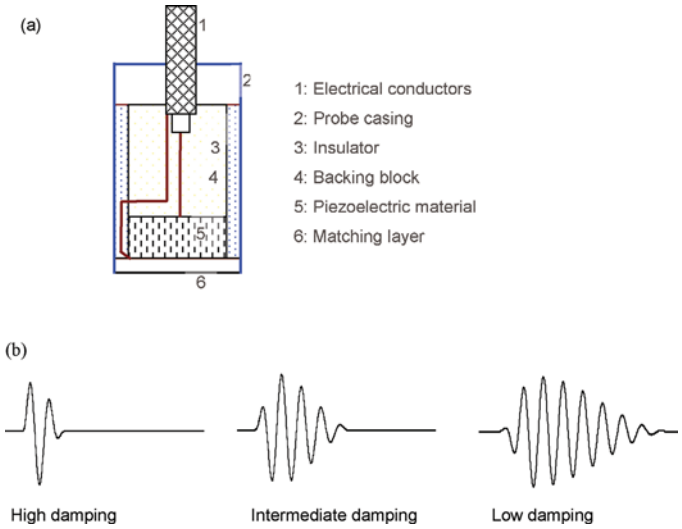

FIG. 2—*Ultrasonic transducer (after Wells 1977): (a) Schematic drawing of a typical single-element ultrasonic transducer, (b) Electronic output from transducers with different backing block subjected to impulse excitation.*

conditions—Wells 1977). The frequency bandwidth is inversely proportional to the duration of ringing.

Backing Block—The extent of ringing is controlled by the backing material. The impedance of the backing material is selected to match that of the piezoelectric material to minimize internal reflections within the piezoelectric element. The backing material adsorbs the transmitted energy and damps it. Typical backing materials include tungsten or rubber powder in an epoxy matrix. Figure 2*b* shows received signals with different levels of transducer damping. In general, the higher the damping is the shorter the signal, the broader the bandwidth, and the lower the amplitude (the lower sensitivity) are.

Matching Layer—The coupling between the piezoelectric element and the medium often involves an intermediate layer, not only for protection but for impedance matching as well. This layer affects the sensitivity and the bandwidth of the transducer. Impedance matching is achieved by selecting a material of intermediate impedance between the target medium and the piezoelectric material, and cutting it into a quarter wavelength λ/4 wave guide (Hadjicostis et al. 1988). Therefore, while the transducer may generate a broad frequency, the matching layer favors the central wavelength, i.e., it acts as a band-pass filter (Zagzebski 1986).

Casing—The mechanical insulator between the probe casing and the piezoelectric element filters external noise. In addition, electromagnetic noise is reduced by grounding the casing.

Selected Transducer—A 0.5 MHz high damping transducer is selected for this research (Panametrics A3441). It includes a matching layer for water, and it is considered as immersion type transducer. The element diameter is 19 mm.

Near Field

The transducer is not a point-source but a disk-shaped piezoelectric element. As Huygen's wavelets radiated from every point on the transducer face travel into the medium, constructive and destructive interferences take place, and a unique pattern of amplitude fluctuations occur in the near field of the transducer. The intensity I_x (which is proportional to the square of the pressure amplitude) at distance x along the central axis of the transducer fluctuates (Krautkramer and Krautkramer 1990),

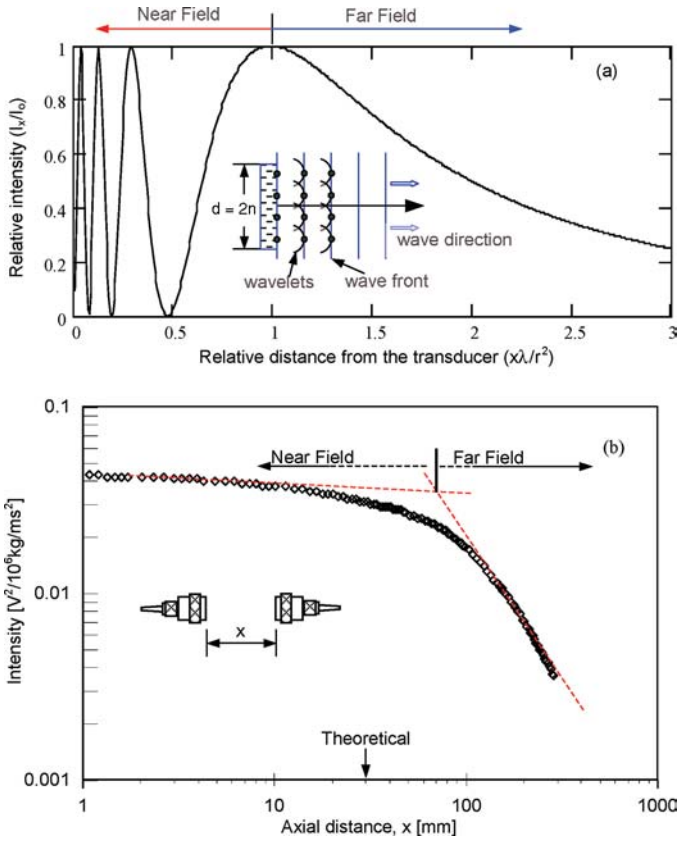

FIG. 3—*Near field: (a) Computed field intensity versus distance at a point along the center line (for d/λ = 8), (b) Signal intensity (peak value) measured with a "pair" of identical transducers versus axial distance along the center line (A34441 transducers).*

$$I_x = I_o \sin^2\left[\frac{\pi}{\lambda}\left\{\sqrt{(r^2+x^2)} - x\right\}\right] \tag{8}$$

where I_o is the intensity at the surface of the transducer and r the radius of the transducer. The variation of the relative intensity I_x/I_o along the centerline is plotted in Fig. 3*a*. The intensity in the near field of the transducer exhibits high spatial fluctuation, and its decay does not follow geometric spreading as shown in Fig. 3*a*. The length of the near field or Fresnel zone x_{NF} is dependent on the transducer radius r and the wavelength λ,

$$x_{NF} = \frac{4r^2 - \lambda^2}{4\lambda} \tag{9}$$

For the $r \gg \lambda$, the length of the near field x_{NF} becomes

$$x_{NF} \approx N = \frac{r^2}{\lambda} = \frac{r^2 f}{V} \quad \text{(single transducer)} \tag{10}$$

Therefore, the extent of the near field x_{NF} increases with increasing transducer size r and increasing frequency f. The theoretically estimated near field length for a single A3441 transducer is ~30 mm (assuming $r = 9.5$ mm, $f = 0.5$ MHz, $V = 1500$ m/s).

Experimental Study—The near field for a pair of identical A3441 transducers is studied by aligning the submerged source and receiver transducers and gradually changing the distance between

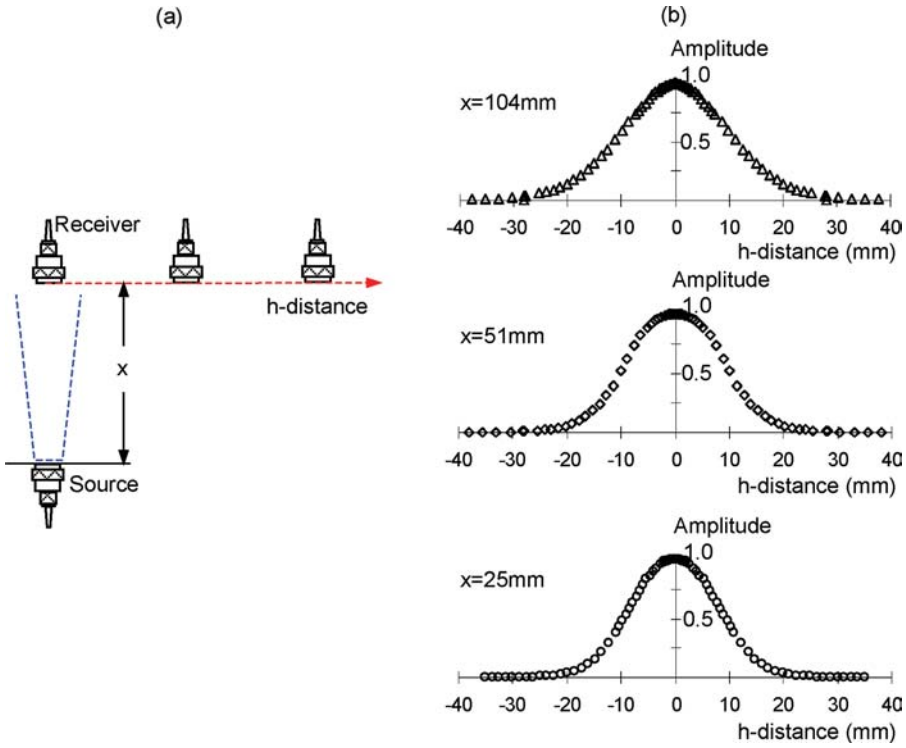

FIG. 4—*Transducer directivity at constant axial distances: (a) Test design, (b) Experimental results. Amplitude is normalized with respect to peak in each case.*

them. The input signal is an impulse (JSR DPT 35). Test results are plotted in Fig. 3*b*. The geometric decay of amplitude versus axial distance becomes apparent when the distance between transducers exceeds ~70 mm. Therefore, this is the effective near field distance for the transducer "pair."

Directivity

A transducer (either a source or a receiver) focuses in certain directions, defining directivity "lobes." The conical bounds of the main lobe where radiated energy vanishes define the divergence angle. The divergence angle should be small to increase lateral resolution. While a focused, low divergence transducer is preferred in medical ultrasound, a wide beam may be preferred to detect off-center reflections with a fixed position transducer.

Experimental Study—The directivity of the selected transducer is studied using the test procedure shown in Fig. 4*a*. The signals are measured at a fixed axial distance, but laterally offsetting the transducers. Experimental results are shown in Fig. 4*b* (a complete dataset can be found in Lee 2003). These results confirm that the selected transducer has strong directivity and small divergence.

Axial Resolution

The axial resolution of the measurement system is studied by gradually changing the distance to a normal planar target using a micrometer. Time differences δt computed from the cross correlation between two stored signals must be $\delta t \geq \Delta t$, where Δt is the sampling interval. For $V_P = 1500$ m/s and sampling frequency ($\Delta t = 1/f_{\text{sampling}} = 1/20$ MHz), the corresponding axial resolution for a two-way travel distance is $\Delta l = V_P \Delta t/2 = V_P/2f_{\text{sampling}} =$ 37.5 μm. However, a better axial resolution can be obtained by phase angle computations in the frequency domain. The time increment calculated from phase angle computation is plotted versus distance in Fig. 5. The attainable axial resolution is about 20 μm.

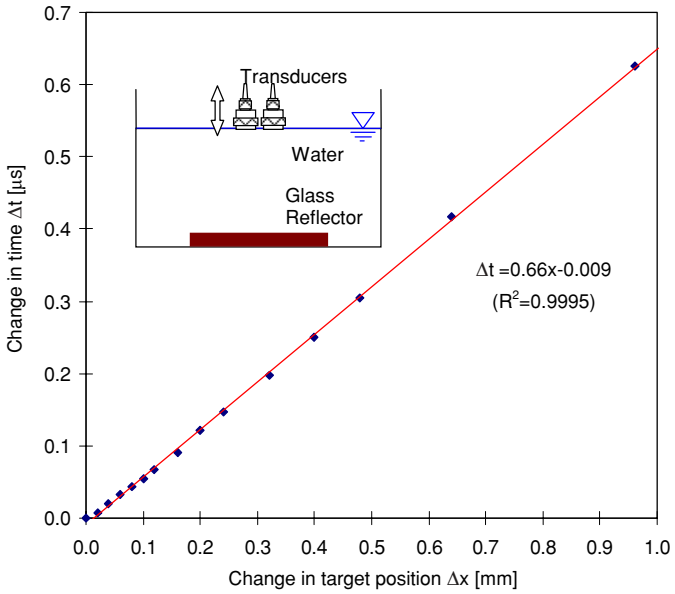

FIG. 5—*Axial resolution–Change in time (from phase difference) versus target position. Initial distance to target ≈125 mm.*

Others: Direct Wave and Water Layer

Direct Wave–Shielding—There is a direct transmission path from the source to the receiver. This path can be intercepted by installing a mechanical shield between the transducers. An effective shield consists of a metal tube placed around the source. Figure 6 shows measured signals with and without the shield.

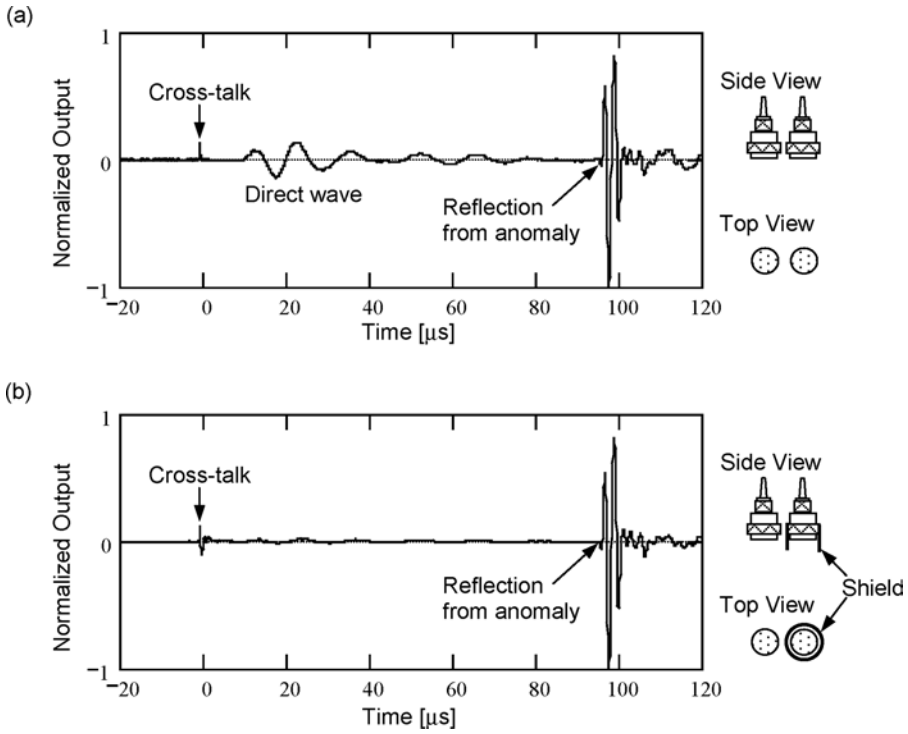

FIG. 6—*Shielding effects: (a) Without shielding, (b) With shielding.*

Water Layer–Optimal Thickness—The water layer thickness between the transducer and the soil surface may vary across applications. Then, the question of optimal thickness arises. In particular, one may seek minimum reflection from the soil-water interface to maximize the energy transferred into the soil. The analytical solution is not trivial, given the compounding effects of near field, directivity, and multiple reflections within the water layer. An experimental parametric study using a sand bed was implemented for this purpose. The amplitude of the measured signal reflected from the water-soil interface (see Fig. 7) is minimum when the interface is less than ~30 mm away from the transducer pair (for a 30-mm center-to-center separation between transducers).

Application Examples

Several unique applications of P-wave monitoring and imaging are explored herein, including: spatial variability and anomaly detection, subsurface monitoring before and after liquefaction, and clay sedimentation.

Spatial Variability

Layers and anomalies can be identified by scanning the surface with the transducer pair to generate a P-wave reflection image. This methodology is explored with the test configuration sketched in Fig. 8*a*. The scanning interval is 1.27 mm to avoid spatial aliasing (wavelength $\lambda = 3$ mm). The thickness of the water layer is selected to minimize the reflection from the water-sand interface. Scanning results are plotted in Fig. 8*b*. Because the divergence of the transducer is small, the anomaly is easily detected without migration. The sand bed is very homogeneous and exhibits no layering. The lower sand-box interface is clearly seen, except where it is "hidden" by the anomaly.

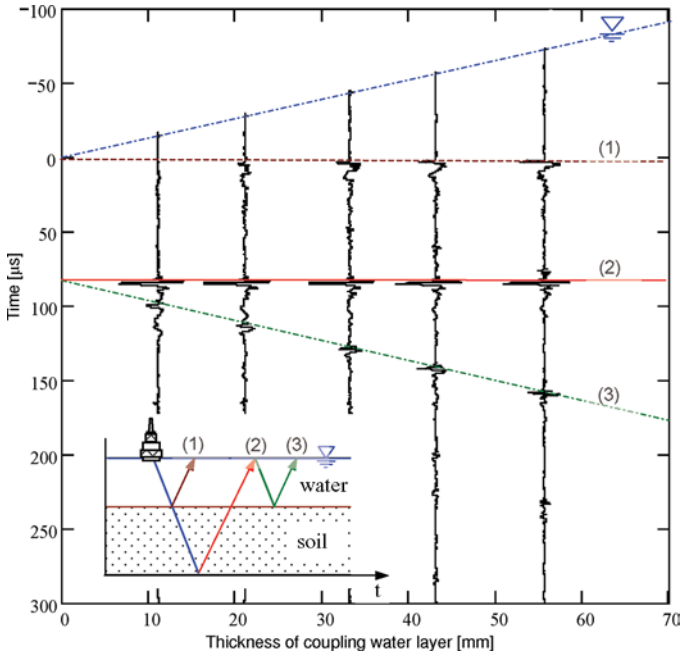

FIG. 7—*Thickness of the coupling water layer. Events 1, 2, and 3 correspond to the multiple reflections shown in the insert. For clarity, the water-soil reflector is shifted to time t = 0.*

Liquefaction Monitoring

A sudden impact can initiate liquefaction in a saturated loose sand bed. Post-liquefaction soil-restructuring causes changes in density, velocity, and impedance, and it may modify soil layering. A low-permeability layer of silica flour is placed within a soil mass as shown in Fig. 9 to simulate common field situations where layering is present. This thin layer acts as a semi-reflective plane. An artificial

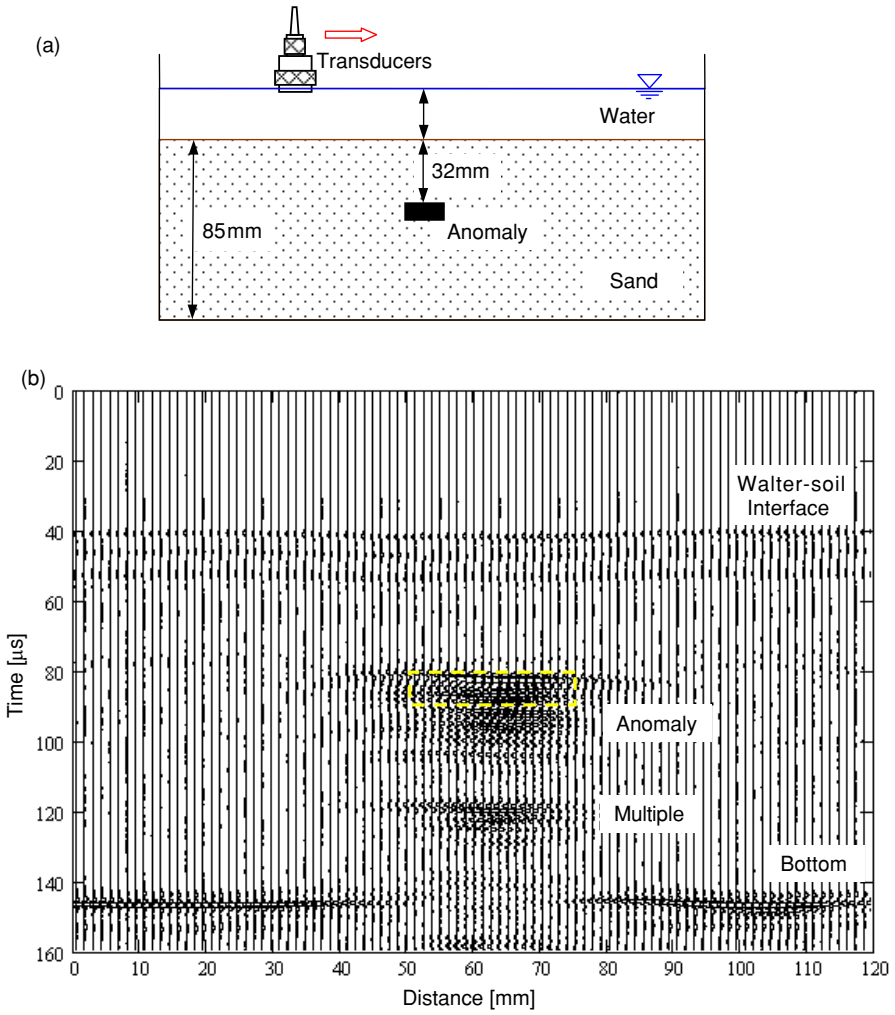

FIG. 8—*Anomaly detection: (a) Test setup, (b) Surface scanning results. Anomaly size: Thickness = 6.33 mm, Width = 25.4 mm, Length = 127 mm.*

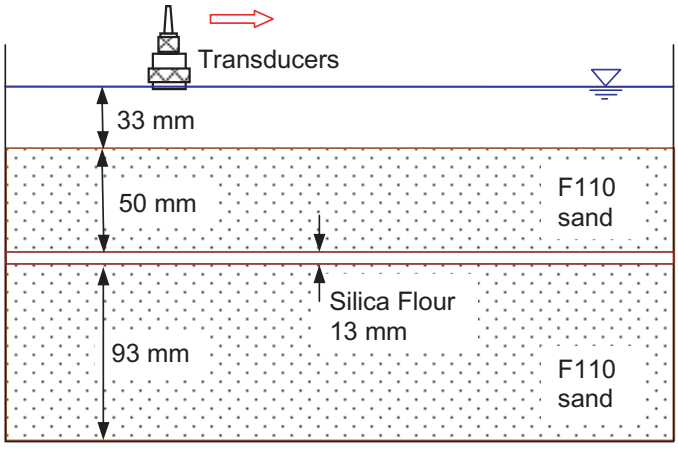

FIG. 9—*Test setup for liquefaction monitoring.*

- The silica flour and the upper sand layer settle after liquefaction due to the densification of the lower sand layer.
- The depression of the soil-water interface and the upper and lower surface of the silt layer provide insightful information about the effect of liquefaction and post liquefaction densification on subsurface deformation.
- The settlement profile is not uniform, and it is biased towards the location of the impact on the left side of the model.
- The amplitude of the P-wave reflected from the bottom of the silica flour layer after liquefaction is larger than the amplitude before liquefaction. This means that the mechanical impedance mismatch between the silica flour and the bottom sand has increased after liquefaction.
- The sign of the reflection coefficient depends on the relative impedance at the interface. The direction of the reflection at the sand-silica interface is opposite to the reflection from the water-sand and silica-sand interfaces.

weak point is created at the center of the specimen to facilitate the dissipation of the excess pore pressure after liquefaction. The reflection images before impacting the soil and two days after liquefaction are presented in Fig. 10. The following observations can be made:

Similar images were obtained several minutes after liquefaction, and the formation of a water gap on the lower surface of the silt layer was readily recognized (see Fiegel and Kutter 1994; Kokuso and Kojima 2002).

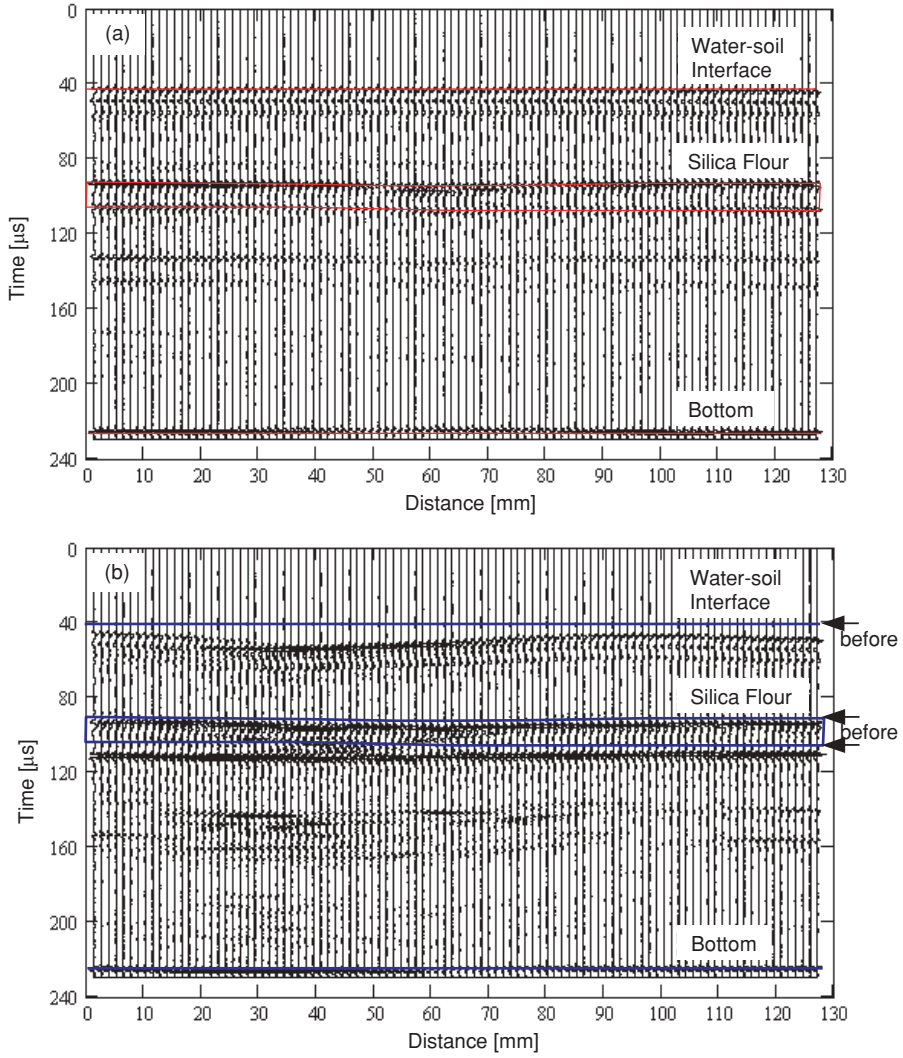

FIG. 10—*P-wave reflection images: (a) Before liquefaction, (b) 2 days after liquefaction; lines indicate soil layers before liquefaction. The void ratio of the silica flour-sand mixture is 7.1 (silica flour is 70 % by weight).*

Clay Sedimentation

Clay sedimentation tests are implemented using kaolinite slurries (RP-2 kaolin—LL = 55 %, other properties in Klein 1999). The slurry is prepared at a water content $w = 490$ %, with a corresponding clay volume fraction of 7.3 %, and it is placed in a 2000 ml graduated cylinder. Sedimentation tests are conducted with and without a dispersing agent (20 g/l of sodium hexametaphosphate) to assess P-wave reflection from different suspension-sediment interface conditions. These tests consist of simultaneously measuring the reflected P-wave signal and recording the visually observed sedimentation height during sedimentation self-weight consolidation.

The optically observed interface settlement versus elapsed time is plotted in Fig. 11*a*. Reflected P-wave signatures from the various interfaces are presented in Figs. 11*b* and *c*. The following observations can be made:

- Clear water-slurry reflections are detected once the interface is at a depth greater than 40 mm in the case of the slurry without dispersing agent, and >90 mm in the slurry with dispersing agent (Fig. 11*b*). Thereafter, the amplitude of this reflection increases as settlement continues.
- Bottom reflections are different in the two slurries (Fig. 11*c*). A single bottom reflector is detected in the slurry without dispersing agent. On the other hand, an additional upward moving slurry-sediment reflection is observed in the slurry with dispersing agent.
- While the P-wave velocity in water is constant, the P-wave velocity in the slurry/sediment may decrease during the initial stages of sedimentation and then increase (see Fig. 1). If the P-wave velocity in water is $V_{P\text{-}W}$ and the depth is l_W, and the P-wave velocity in the slurry is $V_{P\text{-}S}$ and the depth is l_S, then the travel time for the bottom reflector is

$$t = 2\left(\frac{l_w}{V_{P\text{-}W}} + \int_{lw}^{ls+lw} \frac{dz}{V_{P\text{-}S}(z)}\right) \tag{11}$$

Data show that the travel time for the bottom reflector decreases with elapsed time in the slurry with dispersing agent.

Discussion

Gradual Interfaces

The electrical resistance profile is measured at selected times during slurry consolidation using an electrical needle probe to explore

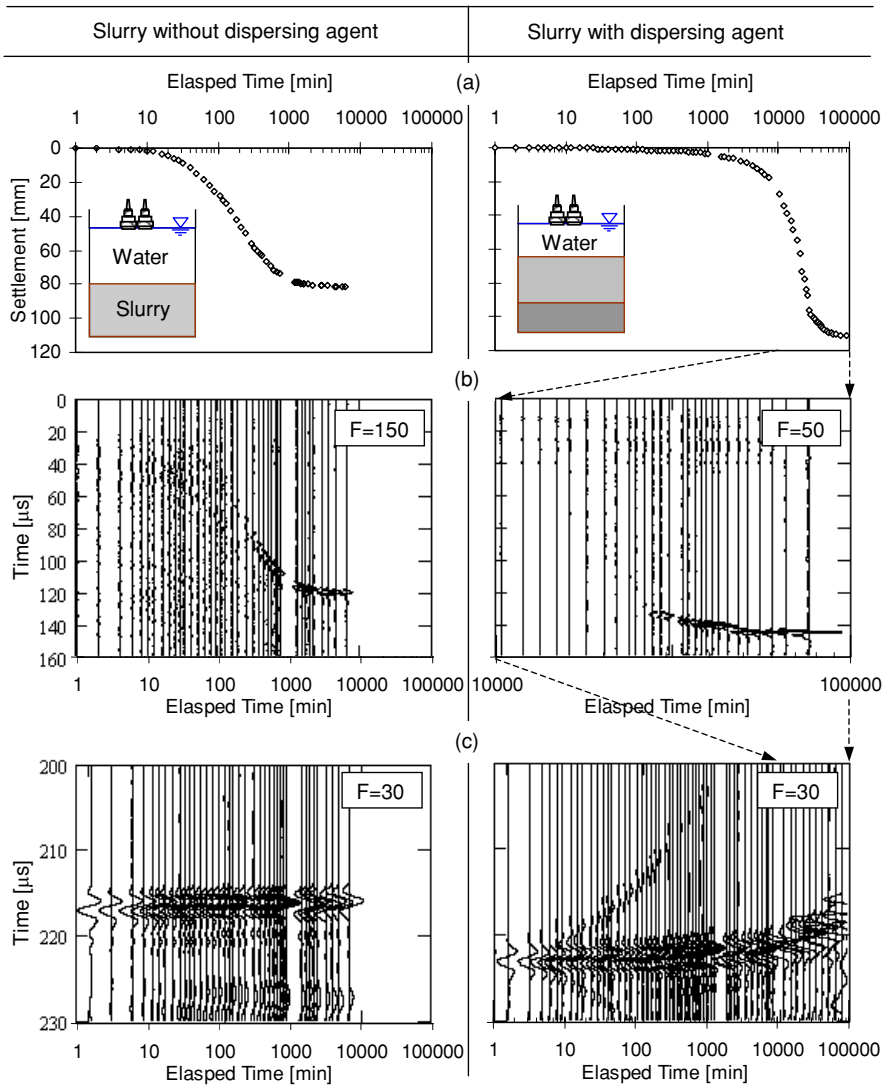

FIG. 11—*Monitoring kaolinte sedimentation: (a) Optically observed interface versus elapsed time, (b) Reflected P-wave at the water-slurry interface, (c) Reflected P-wave from the bottom. F is the amplification factor used in plotting. Note: 100* µs *in water is equivalent to a reflector at a distance of ~75 mm.*

the gradual transition at interfaces (needle design is discussed in Cho et al. 2004). Two resistance profiles and the P-wave signatures determined at the same time are shown in Fig. 12. The electrical resistance profile shows a clear interface between the water and the sediment 2640 min after the sedimentation of the slurry without dispersing agent started (depth ≈88 mm). The companion P-wave signature shows a clear reflection. On the other hand, the slurry with dispersing agent (Fig. 12*b*) shows no clear interface and the P-wave reflection is hindered.

This situation is numerically explored, as shown in Fig. 13. The transition zone is discritized into N layers. The incident wave is recursively reflected at each layer and delayed accordingly. The detailed description of the simulation follows:

1. Discretize the transition zone into N layers;
2. Assign a mean density to each layer and calculate: porosity, V_P (Eq 4), and impedance $z = \rho V_P$ for each layer;
3. Obtain the travel time across each layer ($t = 2L/V_P$);
4. Compute the reflection and transmission coefficients at each interface using Eqs 5 and 6;
5. Sum the time shifted reflected signals (See Aki and Richards 1980; Ben-Menahem and Singh 1981;Mavko et al. 1998). Simulated results are plotted in Fig. 13*c* for different transition lengths L_T normalized by the mean wavelength λ (soil data used in this simulation were gathered from Been and Sills 1981). As the transition length increases, the signal reflection disappears due to the gradual impedance change.

Fresnel Zone

A measured reflection combines energy that returns from any reflector within the ensonification cone (Sheriff and Geldard 1995; Yilmaz 1988). The Fresnel zone is the subsurface area that renders returning energy in-phase. Because constructive interference occurs when a phase difference is less than a half cycle, $\delta\phi < \pi$, the Fresnel zone for a single point source and receiver is computed for a

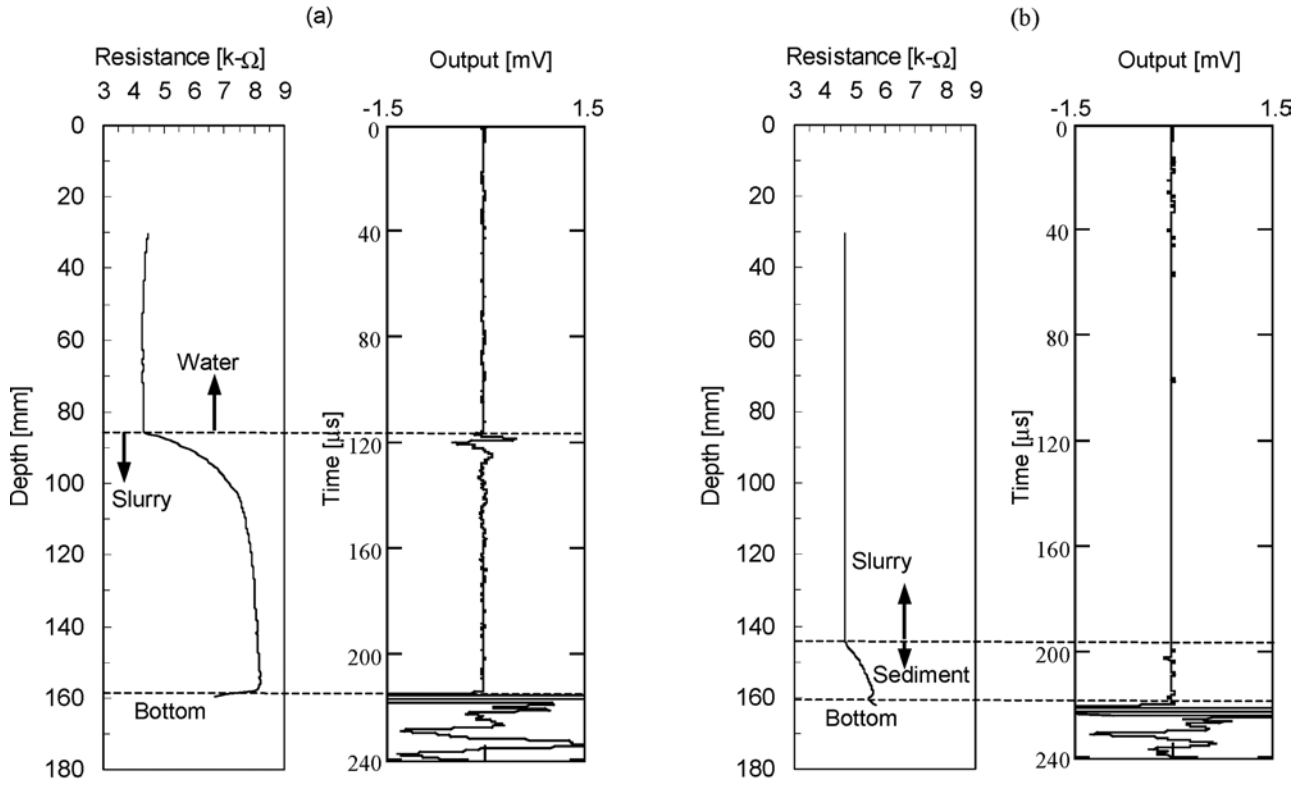

FIG. 12—*Electrical resistivity versus depth and associated P-wave time series: (a) Slurry without dispersing agent, 2640 min (44 h) after clay sedimentation started, (b) Slurry with dispersing agent, 1680 min (28 h) after clay sedimentation started. Electrical needle probe data gathered at f = 100 kHz and 1 V.*

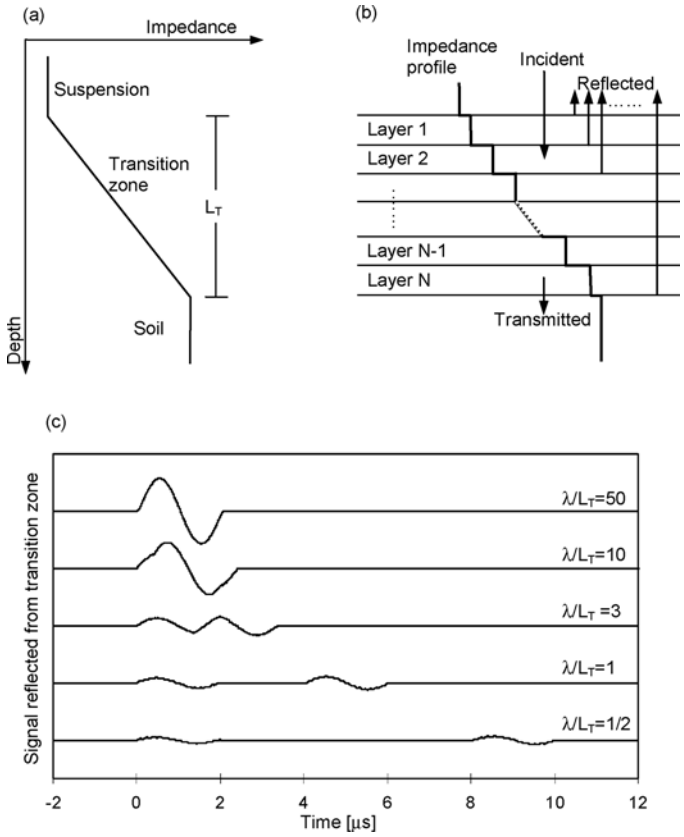

FIG. 13—*P-wave reflection in gradual impedance change media: (a) Impedance profile in transition zone, (b) Multi-layer modeling, (c) Numerical solution. Input: Single cycle sine wavelet.*

one-way travel distance difference of a quarter wavelength λ/4. Then, the radius of the Fresnel zone e is

$$e \approx \sqrt{\frac{x\lambda}{2}} = \sqrt{\frac{xV}{2f}} \tag{12}$$

where x is the depth of the reflector and λ the wavelength. If the frequency f increases, λ decreases, the radius of the Fresnel zone decreases, and the lateral resolution increases. This analysis can be readily extended to the case when the source and the receiver are not at the same point.

Migration

A time series captures reflectors positioned within the ensonification beam. Therefore, P-wave reflection images need to be processed to properly position and size reflectors. This is done by "migration" techniques. The migration of an inclined planar reflector will lead to the following improvements with respect to the apparent image generated with the time series (Yilmaz 1988):

- A steeper angle of the reflector ($\theta_z > \varphi_z$), where θ_z is the inclination of reflector and φ_z is the inclination of the unmigrated section.
- A shorter reflector length.
- A reflector moved along the updip direction.

The measured signal may also result from diffracted signals (Chun and Jacewitz 1981). In this case, migration collapses the diffraction towards the diffractor and increases the spatial resolution. Given the

strong directivity of the transducers used in this study, migration improvements are small and not needed for practical applications.

Conclusions

P-wave reflection imaging techniques permit detecting submerged subsurface layers and inclusions, and monitoring their changes in time. The main observations from this study follow:

- High directivity transducers render high lateral resolution and post-gather migration processing may be unnecessary. However, reflections from tilted reflectors may not be detected unless transducers are pivoted.
- As frequency increases, the axial and lateral resolutions increase, the skin depth decreases, near field length increases, and divergence decreases. Axial resolution requires transducers with high damping. Higher axial resolution is obtained by phase angle determination in the frequency domain.
- The direct wave from the source to the receiver is effectively filtered with a mechanical shield. The depth of the coupling water layer can be optimized to minimize the reflection from the water-soil interface and maximize the energy radiated into the soil.
- Anomalies are clearly detected when they have a high impedance mismatch with respect to the surrounding soil. A highly contrasting anomaly hides the presence of soil layers beneath it.
- Semi-transparent layers permit monitoring subsurface processes. Layer changes and water film formation during liquefaction are clearly detected.
- Clay sedimentation can be effectively monitored using P-wave reflection images. However, the gradual change in impedance at the interface may hinder reflections.

Acknowledgment

This study was supported by the NSF-NEES project, based at the University of California at Davis (directed by Dr. B. L. Kutter), and The Goizueta Foundation.

References

Aki, K. and Richards, P. G., 1980, *Quantitative Seismology—Theory and Methods*, Vols. 1 and 2, Freeman Company, San Francisco.

Been, K. and Sills, G. C., 1981, "Self-weight Consolidation of Soft Soils: an Experimental and Theoretical Study," *Geotechnique*, Vol. 31, No. 4, pp. 519–535.

Ben-Menahem, A. and Singh, S. J., 1981, "Seismic Waves and Sources," 2nd ed., Dover Publications, New York.

Biot, M. A., 1956, "Theory of Propagation of Elastic Waves in Fluid-Saturated Porous Solid. II. Higher Frequency Range," *Journal of the Acoustical Society of America*, Vol. 28, No. 2, pp. 179–191.

Carmichael, R. S., 1982, *Handbook of Physical Properties of Rocks*, CRC Press, Boca Raton.

Carmichael, R. S., 1989, *CRC Practical Handbook of Physical Properties of Rocks and Minerals*, CRC Press.

Cho, G. C., Lee, J. S., and Santamarina J. C., 2004, "Spatial Variability in Soils: High Resolution Assessment with Electrical Needle Probe," *Journal of Geotechnical and Geoenvironmental Engineering,* Vol. 130, No. 8, pp. 843–850.

Chun, J. H. and Jacewitz, C. A., 1981, "Fundamentals of Frequency Domain Migration," *Geophysics*, Vol. 46, No. 5, pp. 717–733.

Fiegel, G. L. and Kutter, B. L., 1994, "Liquefaction Mechanism for Layered Soils," *Journal of Geotechnical Engineering,* Vol. 120, No. 4, pp. 737–755.

Gomm, T. J. and Mauseth, J. A., 1999, "State of the Technology: Ultrasonic Tomography," *Materials Evaluation*, Vol. 57, No. 7, pp. 747–752.

Gueguen, Y. and Palciauskas, V., 1994, *Introduction to the Physics of Rocks*, Princeton University Press, Princeton.

Hadjicostis, A. N., Hottinger, C. F., Rosen, J. J., and Wells, P. N. T., 1988, "Ultrasonic Transducer Materials for Medical Application," *Medical Applications of Piezoelectric Polymers*, Galletti, P. M., De Rossi, D. E., and De Reggi, A. S., Eds., pp. 169–188.

Klein, K., 1999, "Electromagnetic Properties of High Specific Surface Minerals," PhD thesis, Georgia Institute of Technology, Atlanta, Georgia.

Kokusho, T. and Kojima, T., 2002, "Mechanism for Post Liquefaction Water Film Generation in Layered Sand." *Journal of Geotechnical and Geoenvironmental Engineering,* Vol. 128, No. 2, pp. 129–137.

Krautkramer, J. and Krautkramer, H., 1990, "Ultrasonic Testing of Materials," Springer-Verlag, New York.

Lee, J. S., 2003, "High Resolution Geophysical Techniques for Small-Scale Soil Model Testing," PhD Thesis, Georgia Institute of Technology, Atlanta, GA.

Mavko, G., Mukerji, T., and Dvorkin, J., 1998, *The Rock Physics Handbook*, Cambridge University Press, UK.

Mclntire, P., 1991, *Nondestructive Testing Handbook—Ultrasonic Testing*, 2nd ed., American Society of Nondestructive Testing.

Santamarina, J. C., Klein, K. A., and Fam, M. A., 2001, *Soils and Waves—Particulate Materials Behavior, Characterization and Process Monitoring*, John Wiley and Sons, New York.

Sheriff, R. E. and Geldard, L. P., 1995, *Exploration Seismology*, 2nd ed., Cambridge University Press, New York.

Waters, K. H., 1992, *Reflection Seismology: A Tool for Energy Resource Exploration*, 3rd ed., John Wiley & Sons.

Weast, R. C., 1988, *CRC Handbook of Chemistry and Physics*,*First Student Edition*, CRC Press, Boca Raton.

Wells, P. N. T., 1977, *Biomedical Ultrasonics*, Academic Press, New York.

Yilmaz, O., 1988, *Seismic Data Processing*, Society of Exploration Geophysics.

Zagzebski, J. A., 1986, "Essentials of Ultrasound Physics," Mosby, MO.